

# Evolution of Crystallographic Texture of Zirconium Alloy During Hot Deformation

Zeng Qinghui, Luan Baifeng, Chapuis Adrien, Liu Qing

Chongqing University, Chongqing 400044, China

**Abstract:** A hot-rolled and annealed Zr alloy plate of Zr-1.06Sn-0.36Nb-0.3Fe-0.1Cr-0.13O (wt%) was compressed along normal direction (0° sample) and transverse direction (90° sample) at 700 °C and a strain rate of 1 s<sup>-1</sup>. The microstructures and microtextures were characterized by electron backscatter diffraction (EBSD) technique. Visco-plastic self-consistent (VPSC) model was applied to evaluate the activity of slip and twinning systems during deformation at low strain. The results show that dynamic recrystallization (DRX) occurs in the two samples. The texture of the recrystallized grains is similar to that of parent grains, and the preferred nucleation or growth is not in charge of the texture formation. In the 0° sample, all three slip modes (basal, prismatic and pyramidal <c+a> slip) operate at the first stage of deformation, while only a small amount of pyramidal <c+a> slip is active in the 90° sample in the early stage of deformation. The high activity of prismatic slip results in an intensive  $\langle 10\bar{1}0 \rangle // RD$  texture component in the 90° sample. Moreover, predominant basal slip activity at 700 °C is necessary for simulating the observed deformed texture.

**Key words:** zirconium alloy; hot deformation; texture; visco-plastic self-consistent modeling; basal slip

Zirconium (Zr) alloys are widely used in the nuclear industry due to their good mechanical properties and excellent corrosion resistance<sup>[1,2]</sup>. Mechanical properties are strongly anisotropic, depending on the texture formed during the plastic deformation<sup>[3,4]</sup> and annealing treatment<sup>[5,6]</sup>. Zr is a hexagonal close-packed (hcp) metal in which several slip and twinning modes are activated. Up to now, the slip systems observed in Zr alloy include  $\{10\bar{1}0\}\langle 11\bar{2}0 \rangle$  prismatic slip,  $\{0001\}\langle 11\bar{2}0 \rangle$  basal slip,  $\{10\bar{1}1\}\langle 11\bar{2}0 \rangle$  pyramidal <a> slip in the <a> direction, and  $\{10\bar{1}1\}\langle 11\bar{2}3 \rangle$  and  $\{11\bar{2}1\}\langle 11\bar{2}3 \rangle$  pyramidal <c+a> slip<sup>[7-11]</sup>. Because the critical resolved shear stress (CRSS) for the activation of prismatic <a> slip is the lowest<sup>[12]</sup>, this slip is the most easily activated mode. Only the pyramidal <c+a> slip systems are able to accommodate the plastic deformation along the <c> axis of the grains, but require high CRSS. Depending on the strain applied along the <c> axis of a particular crystal, twinning observed in Zr includes  $\{10\bar{1}2\}\langle \bar{1}011 \rangle$  and  $\{11\bar{2}1\}\langle 11\bar{2}6 \rangle$  tension twinning and  $\{11\bar{2}2\}\langle 11\bar{2}3 \rangle$  and  $\{10\bar{1}1\}\langle 10\bar{1}2 \rangle$  compression twinning<sup>[13]</sup>.

Mccabe et al<sup>[3]</sup> reported that different activations of the slip and twinning systems result in different texture evolutions during the deformation of a high-purity Zr at room temperature. Chapuis and Liu<sup>[14]</sup> confirmed that basal slip and pyramidal <a> slip result in a <c> axis rotation toward the compression direction, while pyramidal <c+a> slip contributes to a <c> axis rotation toward the extension direction during the deformation of HCP metals.

Several studies<sup>[5,6,15]</sup> focused on the texture evolution during static recrystallization in Zr alloy. After cold rolling, Zr alloy sheet always exhibits a texture with  $\langle 10\bar{1}0 \rangle$  parallel to the rolling direction (RD)<sup>[16]</sup>. Zhu et al<sup>[5]</sup> found that in the grain growth stage of Zr-2Hf alloy, the  $\langle 10\bar{1}0 \rangle // RD$  texture component disappears, while the  $\langle 11\bar{2}0 \rangle // RD$  component formed at the primary recrystallization stage is strengthened. This texture evolution was due to the preferred growth caused by the stored energy difference between these texture components<sup>[15]</sup>. Moreover, Jedrychowski et al<sup>[17]</sup> claimed that the transition from the  $\langle 10\bar{1}0 \rangle // RD$  component to the

Received date: August 29, 2018

Foundation item: National Natural Science Foundation of China (51531005, 51421001, 51371202); Fundamental Research Funds for the Central University (106112017CDJQJ138803)

Corresponding author: Luan Baifeng, Ph. D., Professor, College of Materials Science and Engineering, Chongqing University, Chongqing 400044, P. R. China, Tel: 0086-23-65106067, E-mail: bfluan@cqu.edu.cn

Copyright © 2019, Northwest Institute for Nonferrous Metal Research. Published by Science Press. All rights reserved.

$\langle 11\bar{2}0 \rangle // RD$  component after partial recrystallization is attributed to the strain induced boundary migration that drives recrystallization in Zr702. Although the influence of temperature and strain rate on the texture evolution during hot deformation in a Zr-Sn alloy has been reported<sup>[18]</sup>, few studies focus on the texture evolution of dynamically recrystallized grains during hot deformation. The plastic strain is imposed on the recrystallized grains during the nucleation and growth processes simultaneously<sup>[19]</sup>. Thus, the texture evolution during hot deformation is more complex than during annealing. Therefore, in the present work, in order to investigate the texture development of the recrystallized grains and the effect of deformation mechanism on the texture evolution during hot deformation, Zr alloy samples with different initial orientations were compressed with different strains. The microtexture was examined using electron backscatter diffraction (EBSD) technique, and slip system activity was calculated by the visco-plastic self-consistent (VPSC) model.

## 1 Experiment

A hot-rolled and annealed Zr-1.06Sn-0.36Nb-0.3Fe-0.1Cr-0.13O (wt%) alloy plate with an initial  $\alpha$  grain size of 15  $\mu\text{m}$  was used. The microstructure and texture of this plate are shown in Fig.1. The Zr alloy sheet exhibits a bimodal texture with (0001) poles lying in the transverse direction (TD)-normal direction (ND) plane, mostly tilted at approximately 20°~30° to the ND. Two types of cylindrical compression specimens with 6 mm in diameter and 6 mm in height were cut from the plate: the axial direction of the first samples was parallel to the plate ND, and that of the second samples was parallel to the plate TD (Fig.2); these two samples are hereafter designed as the 0° sample and the 90° sample, respectively. In the 0° sample and 90° sample, the  $\langle c \rangle$ -axes of the grains were almost parallel and nearly perpendicular to the loading direction of the sample, respectively. Compression experiments were performed at 700 °C in vacuum at 1 s<sup>-1</sup> strain rate, using a Gleeble-3500 thermal simulator. After compression, the samples were immediately quenched by a water jet. The microstructure was observed at the center of the compression axis-RD of the original plate using a Tescan Mira 3-XMU scanning electron microscope (SEM) equipped with a backscatter electron detector and an EBSD analysis system (AZtec, Oxford Instruments).

## 2 Visco-Plastic Self-consistent Modeling

The visco-plastic self-consistent (VPSC) model associated with the predominant twin reorientation scheme (VPSC-PTR) has not only been used to simulate the deformation of Zr at low temperature and room temperature<sup>[4]</sup>, but also at high temperature<sup>[12]</sup>. The VPSC-PTR<sup>[20]</sup> was applied to simulate the uniaxial deformation tests in this study. Here, only a short

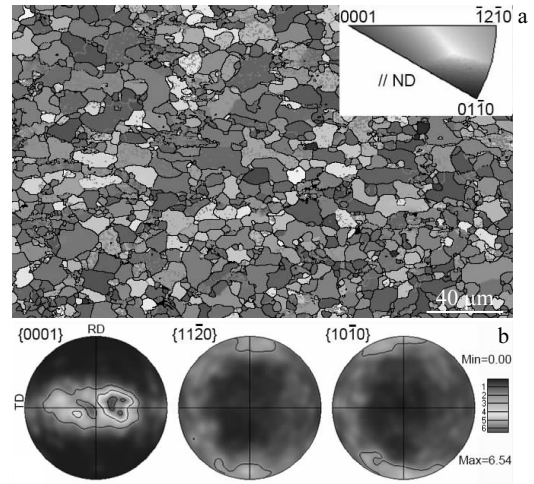


Fig.1 EBSD inverse pole figure (IPF) maps in ND (a) and pole figures (b) of the as-received plate

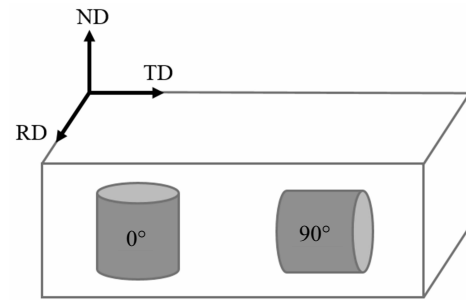


Fig.2 Method for sampling from original plate

description is given to correlate the equations with the parameters used in this study. Regardless of slip and twinning, the shear strain rate is defined as:

$$\dot{\gamma}^{\alpha} = \dot{\gamma}^0 \left| \tau^{\alpha} / \tau_c^{\alpha} \right|^{\frac{1}{m}} \text{sgn}(\tau^{\alpha}) \quad (1)$$

where  $\dot{\gamma}^0$ ,  $\tau_c^{\alpha}$  and  $m$  are reference shear rate ( $\dot{\gamma}^0 = 1 \text{ s}^{-1}$ ), threshold stress which is initially equal to the CRSS, and the strain rate sensitivity, respectively.

The local strain rate tensor is obtained by Eq.(2):

$$\dot{\epsilon} = \sum_{\alpha} P^{\alpha} \cdot \dot{\gamma}^{\alpha} = \sum_{\alpha} \dot{\gamma}^0 \cdot P^{\alpha} \cdot \left( \frac{P^{\alpha} : \sigma}{\tau_c^{\alpha}} \right)^{\frac{1}{m}} \quad (2)$$

where  $\dot{\epsilon}$  is the strain rate tensor (setting  $\dot{\epsilon}_{ii} = 1$  along the loading direction, equal to the experimental strain rate) and  $\sigma$  is the Cauchy stress tensor.  $P^{\alpha} = (s^{\alpha} n^{\alpha} + n^{\alpha} s^{\alpha}) / 2$  is the Schmid tensor, where  $s^{\alpha}$  and  $n^{\alpha}$  are the slip and twinning direction, respectively, normal to the slip or twinning plane.

For both slip and twinning, the evolution of the threshold stress  $\tau_c^{\alpha}$  (or CRSS) is characterized by a Voce hardening law:

$$\tau_c^\alpha = \tau_0^\alpha + (\tau_1^\alpha + \theta_1^\alpha \Gamma) [1 - \exp(-\frac{\theta_0^\alpha}{\tau_1^\alpha} \Gamma)] \quad (3)$$

where  $\tau_0$ ,  $\theta_0$ ,  $\theta_1$  and  $\tau_0 + \tau_1$  are the initial CRSS, initial hardening rate, asymptotic hardening rate, and back-extrapolated CRSS, respectively. Self and latent hardening are indistinguishable so set to 1.

The VPSC-PTR model with the affine self-consistent scheme was employed in the following simulation. The initial rolled texture consisted of 2000 discrete orientations. It was assumed that the plastic deformation is accommodated by prismatic ( $\{10\bar{1}0\}\langle 11\bar{2}0 \rangle$ ), basal ( $\{0001\}\langle 11\bar{2}0 \rangle$ ), and pyramidal  $\langle c+a \rangle$  ( $\{10\bar{1}1\}\langle 11\bar{2}3 \rangle$ ) slips, tensile twinning ( $\{10\bar{1}2\}\langle \bar{1}011 \rangle$ ) as well as compression twinning ( $\{10\bar{1}1\}\langle 10\bar{1}2 \rangle$ )<sup>[12]</sup>.

A threshold twin volume fraction is defined in the PTR model to initiate twinning, because at low strain, parent grains tend to deform more by twinning whereas twins do not deform. Two statistical variables are used: accumulated twin fraction  $V^{\text{acc}}$  and effective twinned fraction  $V^{\text{eff}}$ . More specifically,  $V^{\text{acc}}$  and  $V^{\text{eff}}$  are the weighted volume fraction of the twinned region and volume fraction of twin terminated grains (i.e. grains reoriented into twins), respectively. The threshold volume fraction  $V^{\text{th}}$  is defined as:

$$V^{\text{th}} = A^{\text{th}1} + A^{\text{th}2} \left( \frac{V^{\text{eff}}}{V^{\text{acc}}} \right) \quad (4)$$

where  $A^{\text{th}1}$  and  $A^{\text{th}2}$  are two artificial material constants, empirically determined but with no physical meaning. The PTR parameters  $A^{\text{th}1}$  and  $A^{\text{th}2}$  were fixed so that  $V^{\text{acc}} \approx V^{\text{eff}}$ ,  $\{10\bar{1}2\}$  and  $\{10\bar{1}1\}$  twins were not allowed to endure secondary twinning, although the two twins could co-exist in the same grain.

### 3 Results

#### 3.1 True stress-strain curves

Fig.3 shows the true stress-true strain curves of the two samples deformed at 700 °C and a strain rate of 1 s<sup>-1</sup>. For the 0° sample, the flow stress increased rapidly and reached a peak stress at a relatively low strain. After the peak stress, the flow stress decreased with increasing strain. This is a classic dynamic recrystallization (DRX) flow curve. For the 90° sample, the flow stress increased slowly and then decreased slightly, which corresponds to a typical dynamic recovery (DRV) flow curve. In the early stage of deformation, the flow stress of 0° sample is clearly higher than that of 90° sample.

#### 3.2 Microstructure and texture development

Fig.4 shows the internal average misorientation angle (IAMA) distribution maps for the two samples deformed to a strain of approximately 0.8. In the present study, if the IAMA in a grain is below 2°, this grain is classified as recrystallized grain. Some grains are constituted of subgrains, and the IAMA in the subgrains is below 2°, but the misorientation between the subgrains is above 2°. In this case, the grain is classified as

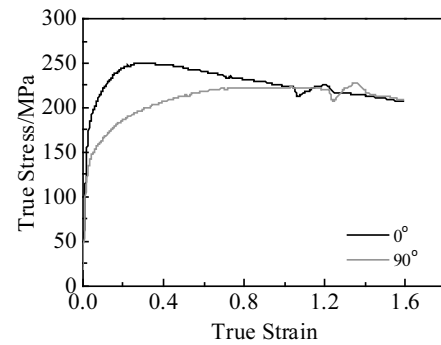


Fig.3 True stress-true strain curves of the two samples deformed at 700 °C

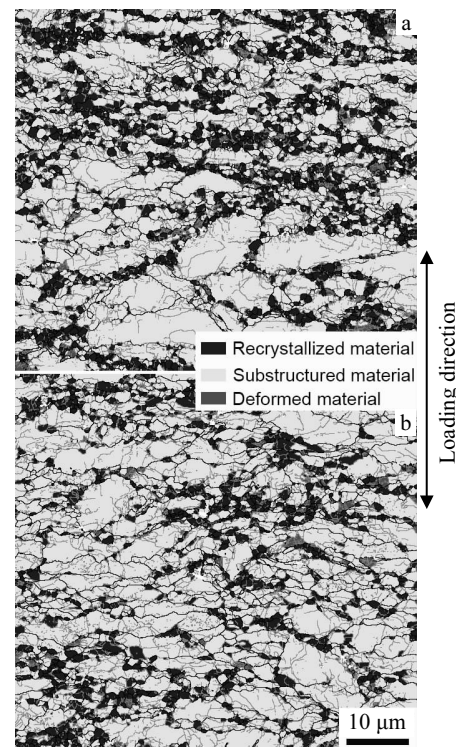


Fig.4 Internal average misorientation distribution maps for 0° sample deformed to a strain of 0.80 (a) and 90° sample deformed to a strain of 0.84 (b) (high-angle boundaries, HABs misorientation  $\theta > 15^\circ$ , and low-angle boundaries, LABs  $2^\circ < \theta < 15^\circ$ , are marked by black and gray lines, respectively)

substructured grain. The remaining grains are classified as deformed grains. As shown in Fig.4, a moderate amount of recrystallized grains represented in blue can be found in the two samples, indicating that DRX occurs in the two samples. As reported in previous study<sup>[21]</sup>, in a 90° sample, the grains rotate from soft orientations ( $\langle c \rangle$ -axis oriented at 70° to the loading direction) to hard orientations in the early stage of deformation. Therefore, texture-induced hardening also occurs, which

compensates the softening induced by DRX, resulting in a typical DRV flow curve in the 90° sample (Fig.3). Moreover, the recrystallized grains are formed along the original grain boundaries, which is a classical feature of DRX. This observation is in agreement with the reported study on a Zr-1Nb alloy<sup>[22]</sup>.

Fig.5 shows the pole figures for the recrystallized grains and parent grains in the 0° sample deformed to different strains. It

can be seen that the texture of the recrystallized grains is similar to that of the parent grains, showing a typical Zr alloy bimodal basal texture. In the  $\{10\bar{1}0\}$  and  $\{11\bar{2}0\}$  pole figures, two weak components  $\langle 10\bar{1}0 \rangle // RD$  and  $\langle 11\bar{2}0 \rangle // RD$  coexist. With increasing strain, the texture does not change remarkably. Fig.6 shows the pole figures for the recrystallized grains and parent grains in the 90° sample deformed to different strains. The similar texture components are found in the pole figures of

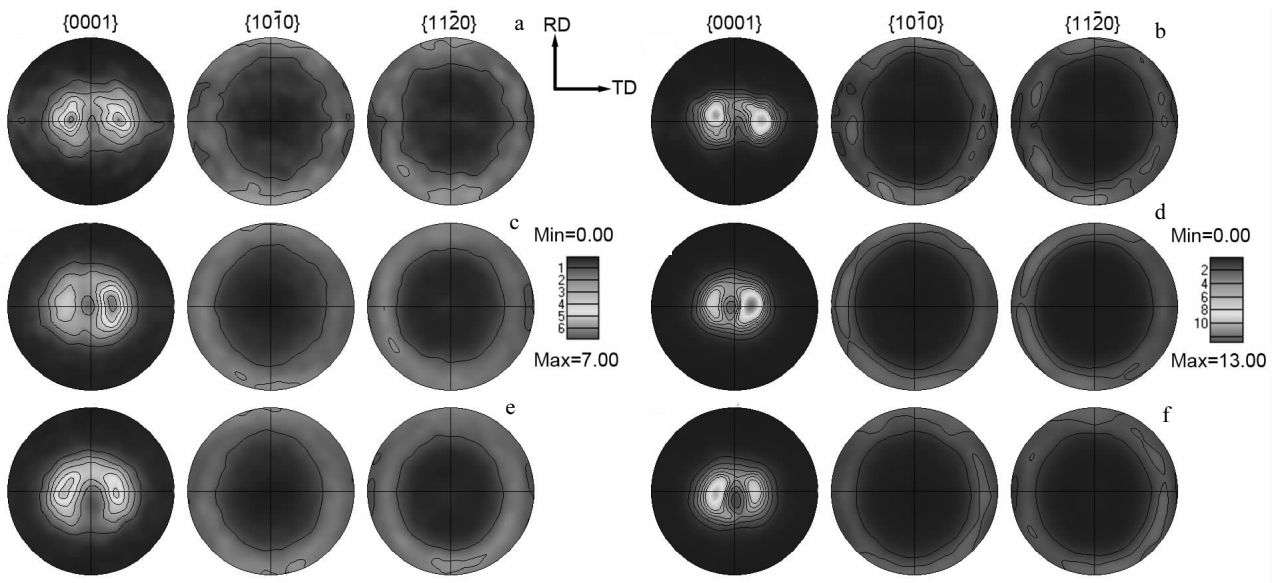


Fig.5 Pole figures for the recrystallized grains (a, c, e) and the parent grains (b, d, f) in 0° sample deformed to different strains: (a, b) 0.53, (c, d) 0.80, and (e, f) 1.27 (ND is the loading direction; RD is the rolling direction of the original plate)

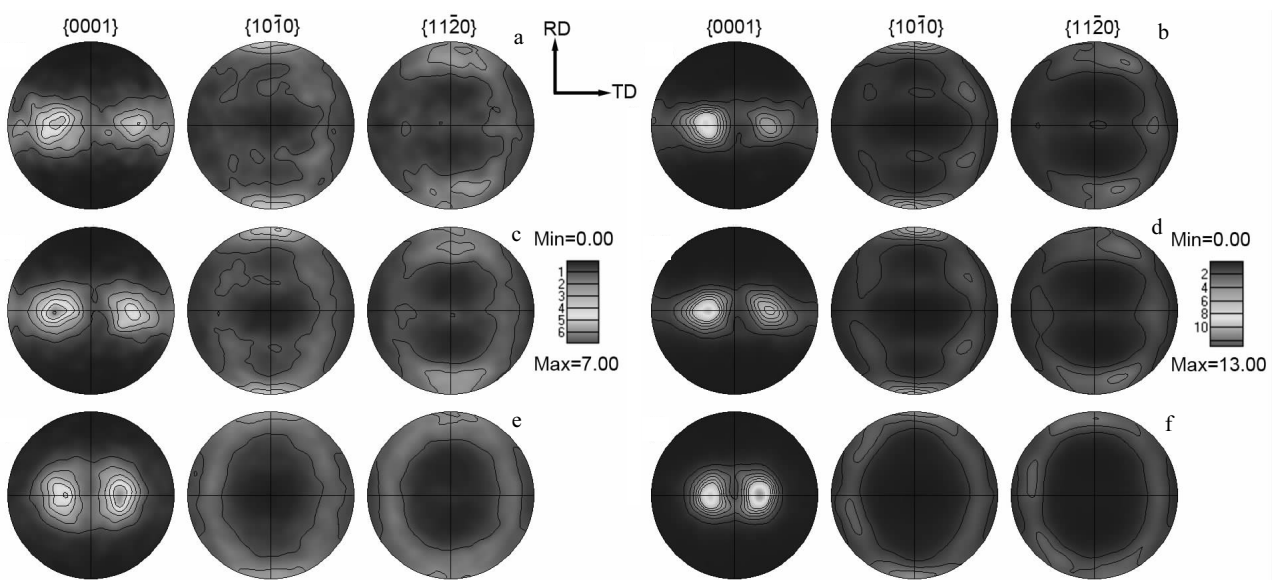


Fig.6 Pole figures for the recrystallized grains (a, c, e) and the parent grains (b, d, f) in 90° sample deformed to different strains: (a, b) 0.56, (c, d) 0.84, and (e, f) 1.24 (ND is the loading direction; RD is the rolling direction of the original plate)

recrystallized grains and parent grains, including the bimodal basal texture component,  $\langle 10\bar{1}0 \rangle //RD$  component and  $\langle 11\bar{2}0 \rangle //RD$  component. A noticeable difference between the two samples is that the  $\langle 10\bar{1}0 \rangle //RD$  component is stronger in the  $90^\circ$  sample. As the strain increases to 1.24, the  $\langle 10\bar{1}0 \rangle //RD$  component becomes weaker than at low strain.

### 3.3 VPSC simulation

Compression tests were performed at 1 and  $0.001 \text{ s}^{-1}$  [21] to obtain the strain rate sensitivity. The strain rate sensitivity parameter  $m$  in Eq.(1) was calculated from the experiments by Eq.(5) using the experimental stress  $\sigma_i$  corresponding to strain rate  $\dot{\epsilon}_i$ , at different strains for the  $0^\circ$  and  $90^\circ$  samples. The calculated strain rate sensitivity parameter of the two samples was between  $m=0.16$  and  $m=0.2$ . Consequently, an average value of  $m=0.167$  (i.e. rate sensitivity exponent  $n=1/m=6$ ) was chosen for the simulation, with the same value for all slip and twinning modes. Table 1 shows the material parameters used in the VPSC simulation. The observed twin volume fraction was lower than 2%, so the CRSSes for twinning modes were assigned high values in order to minimize twinning activity. The material parameters (CRSS) were adjusted to fit the two stress-strain curves and to reproduce the observed texture. Relatively low CRSS values were necessary to rotate  $\langle c \rangle$  toward the compression direction in the  $90^\circ$  sample, but a too low ratio of  $\tau^{\text{basal}}/\tau^{\langle c+a \rangle}$  would make the (0001) poles of the bimodal texture in the  $0^\circ$  sample too close.

$$m = \frac{1}{n} = \frac{\ln(\sigma_1 / \sigma_2)}{\ln(\dot{\epsilon}_1 / \dot{\epsilon}_2)} \quad (5)$$

The experimental and simulation loading curves, experimental and predicted  $\{0001\}$ ,  $\{11\bar{2}0\}$  and  $\{10\bar{1}0\}$  pole figures at a strain of 0.31 for the two samples are shown in Fig.7 and Fig.8, respectively. The calculated texture results are in agreement with the experimental results, abstraction made of the nonsymmetric nature of the bimodal texture. This result indicates that the chosen relative CRSS and the VPSC model can be used to model the deformation of Zr alloys at  $700^\circ\text{C}$  and low strain. In previous studies, crystal plasticity modeling [23] and elasto-plastic self-consistent modeling [24] have been applied to analyze the activity of slip and twinning systems in Zr alloy deformed at temperatures of  $500^\circ\text{C}$  and  $550^\circ\text{C}$ . The present results show that VPSC modeling can be extended to higher temperatures. Fig.9 shows the activity of slip and twinning systems in the two samples. In the  $0^\circ$  sample, basal slip significantly contributes to the deformation, and prismatic and pyramidal  $\langle c+a \rangle$  slips equally accommodate the compressive strain. For the  $90^\circ$  sample, prismatic slip contributes significantly to the deformation; although the relative activity of basal slip is less than that of the prismatic slip, basal slip is also important to the deformation, and it is worth noting that the activity of pyramidal  $\langle c+a \rangle$  slip in  $90^\circ$  sample is much lower than that in  $0^\circ$  sample.

## 4 Discussion

### 4.1 Basal slip at $700^\circ\text{C}$

As shown in Fig.9, basal slip plays an important role during the deformation of the two samples at  $700^\circ\text{C}$ , whereas basal slip has a high CRSS value and does not occur in single crystals at room temperature [7]. In previous work, basal slip was considered as the hardest to activate among the three common  $\langle a \rangle$  slip systems (prismatic, pyramidal and basal slips) in Zr and its alloys. And this has been confirmed by experimental [7] and modeling [4] results at ambient temperature with low strain, and albeit basal slip has been observed near cracks [7,25], kink bands and twins [26]. Knezevic et al [27] reported that a large amount of basal slip activities result in the classical rolling texture in Zr deformed to large strain at ambient conditions, but the strain in their study is much higher than that in the present work. Gurao et al [28] also claimed that basal slip operates at high strain in pilgering of Zircaloy-4. On the other hand, by polycrystalline model, several researchers [29,30] found that models including basal slip can fit better with the experimental flow curves and textures. However, some other studies [31] have also shown a good agreement between the experimental and modeling results using pyramidal  $\langle a \rangle$  slip instead of basal slip. In the current work, using pyramidal  $\langle a \rangle$  slip instead of basal  $\langle a \rangle$  slip does not result in the desired texture.

Recently, Knezevic et al [12] found that basal slip is favored at high temperature. Consistent with their study, in our work,

**Table 1** Material parameters used in the VPSC simulation

Mode	$\tau_0/\text{MPa}$	$\tau_1/\text{MPa}$	$\theta_0/\text{MPa}$	$\theta_1/\text{MPa}$	$A^{\text{th1}}$	$A^{\text{th2}}$
Prismatic slip	25	20	100	0	-	-
Basal slip	40	35	100	0	-	-
Pyramidal $\langle c+a \rangle$ slip	135	40	300	0	-	-
Tensile twin	200	1	200	100	0.2	0.1
Compression twin	300	1	200	100	0.2	0.1

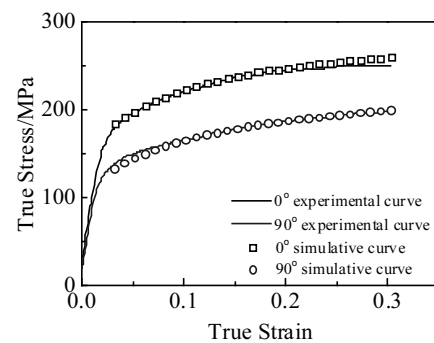


**Fig.7** Experiment and simulation loading curves for  $0^\circ$  and  $90^\circ$  samples at  $1 \text{ s}^{-1}$

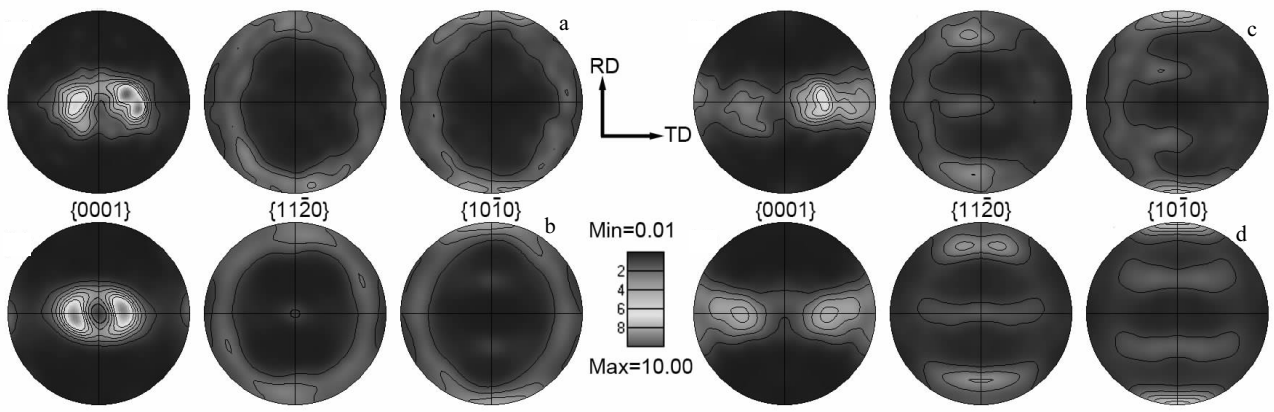


Fig.8 Experiment (a, c) and simulation (b, d) pole figures for the two samples deformed to a strain of 0.31: (a, b) 0° sample and (c, d) 90° sample (ND is the loading direction, RD is the rolling direction of the original plate)

substantial amount of basal slips contribute to the plastic deformation. Predominant basal slip activity at 700 °C can be attributed to its low CRSS value at high temperature.

#### 4.2 Texture

The results reveal that the texture of the recrystallized grains follows that of the parent grains. This observation is in agreement with that reported by Cottam<sup>[32]</sup>, who performed texture analysis of the recrystallized grains and parent grains in pure magnesium and three Mg-Y alloys under plane strain compression deformation. However, some studies<sup>[5,6]</sup> indicated that reoriented recrystallization nucleation indeed occurs in Zr alloy. During the hot deformation, the grain rotation is mainly governed by the plastic strain, and thus the orientation of the recrystallized grains follows that of the parent grains. As a result, the texture of recrystallized grains is similar to that of parent grains. In this work, we also found that the  $\langle 10\bar{1}0 \rangle //$  RD texture component is strengthened in the 90° sample compared with in the 0° sample. Since the preferred nucleation or growth is not in charge of the texture formation, this discrepancy is mainly attributed to the different activity requirements of slip systems in the two samples. Chapuis and Liu<sup>[14]</sup> reported that prismatic slip causes a rotation of the prismatic plane toward the extension direction. More strain was accommodated along the RD than along the ND, indicating that the RD is the extension direction in the 90° sample<sup>[33]</sup>. So the higher activity of prismatic slip in the 90° sample (Fig.9) resulted in an intensive  $\langle 10\bar{1}0 \rangle //$  RD texture component. In the 90° sample, with increasing strain, more and more grains'  $\langle c \rangle$  axes tilt is close to the loading direction, and this orientation is unfavorable for the activation of prismatic slip. Thus, some other modes, such as basal and pyramidal  $\langle c+a \rangle$  slips, mainly accommodate the deformation at high strain. So the lower activity of prismatic slip leads to the weaker  $\langle 10\bar{1}0 \rangle //$  RD texture component in the 90° sample at high strain.

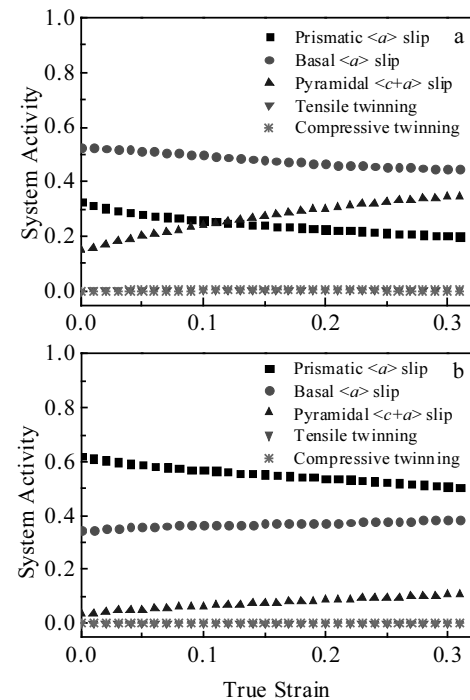


Fig.9 Activity of slip and twinning systems in 0° (a) and 90° (b) samples

## 5 Conclusions

- 1) Basal slip is favored at 700 °C, which mainly causes the texture evolution.
- 2) The development of texture for the recrystallized grains is mainly governed by the plastic strain, resulting in a similar texture of the recrystallized grains and the parent grains in the two samples.
- 3) The intensive  $\langle 10\bar{1}0 \rangle //$  RD texture component in 90° sample is attributed to the high activity of prismatic slip.

## References

- 1 Linga Murty K, Charit I. *Progress in Nuclear Energy*[J], 2006, 48(4): 325
- 2 Zou Dongli, Luan Baifeng, Xiao Dongping. *Rare Metal Materials and Engineering*[J], 2014, 43(8): 1897 (in Chinese)
- 3 McCabe R J, Proust G, Cerreta Ellen K et al. *International Journal of Plasticity*[J], 2009, 25(3): 454
- 4 Tomé C N, Maudlin P J, Lebensohn R A et al. *Acta Materialia*[J], 2001, 49(15): 3085
- 5 Zhu K Y, Chaubet D, Bacroix B et al. *Acta Materialia*[J], 2005, 53(19): 5131
- 6 Gerspach F, Bozzolo N, Wagner F. *Scripta Materialia*[J], 2009, 60(4): 203
- 7 Akhtar A. *Acta Metallurgica*[J], 1973, 21(1): 1
- 8 Akhtar A. *Metallurgical Transactions A*[J], 1975, 6(6): 1217
- 9 Akhtar A. *Journal of Nuclear Materials*[J], 1973, 47(1): 79
- 10 Akhtar A. *Scripta Metallurgica*[J], 1975, 9(8): 859
- 11 Akhtar A, Teghtsoonian A. *Acta Metallurgica*[J], 1971, 19(7): 655
- 12 Knezevic M, Zecevic M, Beyerlein Irene J et al. *Acta Materialia*[J], 2015, 88: 55
- 13 Capolungo L, Marshall P E, McCabe R J et al. *Acta Materialia*[J], 2009, 57(20): 6047
- 14 Chapuis A, Liu Q. *Computational Materials Science*[J], 2015, 97: 121
- 15 Zhu K Y, Bacroix B, Chauveau T et al. *Metallurgical and Materials Transactions A*[J], 2009, 40(10): 2423
- 16 Tenckhoff E. *Zirconium in the Nuclear Industry: 14th International Symposium*[C]. Pennsylvania: American Society Testing and Materials, 2005: 25
- 17 Jedrychowski M, Bacroix B, Salman O U et al. *IOP Conference Series: Materials Science and Engineering*[J], 2015, 89: 12 029
- 18 Jha S K, Keskar N, Narayan K I V et al. *Journal of Nuclear Materials*[J], 2016, 482: 12
- 19 Sakai T, Belyakov A, Kaibyshev R et al. *Progress in Materials Science*[J], 2014, 60: 130
- 20 Lebensohn R A, Tomé C N. *Acta Metallurgica et Materialia*[J], 1993, 41(9): 2611
- 21 Luan B F, Li X Y, Zhang M et al. *Materials Research Innovations*[J], 2014, 18(S4): 1095
- 22 Sarkar A, Chandanshive Sandeep A, Thota Manoj K et al. *Journal of Alloys and Compounds*[J], 2017, 703: 56
- 23 Honniball Peter D, Preuss M, Rugg D et al. *Metallurgical and Materials Transactions A*[J], 2015, 46(5): 2143
- 24 Evans C, Jones Nicholas G, Rugg D et al. *Journal of Nuclear Materials*[J], 2012, 424(1-3): 123
- 25 Yoo M H. *Metallurgical Transactions A*[J], 1981, 12(3): 409
- 26 Martin J L, Reedhill R E. *Transactions of the Metallurgical Society of AIME*[J], 1964, 230(4): 780
- 27 Knezevic M, Beyerlein Irene J, Nizolek T et al. *Materials Research Letters*[J], 2013, 1(3): 133
- 28 Gurao N P, Akhiani H, Szpunar J A. *Journal of Nuclear Materials*[J], 2014, 453(1-3): 158
- 29 Pang J W L, Holden T M, Turner P A et al. *Acta Materialia*[J], 1999, 47(2): 373
- 30 Francillette H, Bacroix B, Gasperini M et al. *Acta Materialia*[J], 1998, 46(12): 4131
- 31 Tomé C N, Lebensohn R A, Kocks U F. *Acta Metallurgica et Materialia*[J], 1991, 39(11): 2667
- 32 Cottam R, Robson J, Lorimer G et al. *Materials Science and Engineering A*[J], 2008, 485(1-2): 375
- 33 Luan B F, Gao S S, Chai L J et al. *Materials & Design*[J], 2013, 52: 1065

## 锆合金热变形过程中的织构演变

曾庆辉, 栾佰峰, Chapuis Adrien, 刘 庆

(重庆大学, 重庆 400044)

**摘要:** 选取了一种热轧退火态的锆合金板材沿着其板材法向(0°样品)及横向(90°样品)在700 °C下以1 s<sup>-1</sup>应变速率进行压缩试验。利用电子背散射衍射(EBSD)技术对变形后样品的微观组织及织构进行表征, 并利用粘塑性自洽模型(VPSC)确定了在低应变条件下的各滑移系及孪晶的相对开启量。微观组织揭示了在2种样品中均有动态再结晶的发生。再结晶晶粒的织构变化与变形晶粒的织构变化相似, 表明再结晶过程中的优先形核及长大过程不会影响织构的形成及变化。在0°样品中, 基面滑移、柱面滑移和锥面<c+a>滑移在变形初期阶段同时开启, 但是在90°样品中, 只有少量的锥面<c+a>滑移在变形初期阶段开启。在90°样品中存在的高强度{10-10}//RD织构组分是由大量开启的柱面滑移造成的。此外, 700 °C下大量基面滑移的开启对织构形成起重要作用。

**关键词:** 锆合金; 热变形; 织构; 粘塑性自洽模拟; 基面滑移

作者简介: 曾庆辉, 男, 1991年生, 博士, 重庆大学材料科学与工程学院, 重庆 400044, 电话: 023-65106067, E-mail: zengqinghui@cqu.edu.cn